Available online at www.sciencedirect.com
ScienceDirect
International Journal of Heat and Mass Transfer 50 (2007) 464–478
International Journal of HEAT and MASS TRANSFER
www.elsevier.com/locate/ijhmt

Layered porous media architecture for maximal cooling

Philippe Wildi-Tremblay, Louis Gosselin *

Département de génie mécanique, Université Laval, Québec, Canada, G1K 7P4

Received 14 December 2005; received in revised form 23 July 2006
Available online 17 October 2006

Abstract

In this paper, we address the fundamental problem of how to arrange fluid flow and solid material for minimal thermal resistance. A heat-generating board is cooled by a stack of porous layers through which a coolant flows. The stream is generated by a fixed pressure drop. The problem consists in determining the optimal porosity and material of each layer for minimizing the hot spot temperature (thermal resistance), under global mass and cost constraints. We combine a genetic algorithms (GA) toolbox with a finite volume program to optimize the design. The shape and structure of the system emerge from the global optimization, under global constraints. The optimal material to use in each layer is determined by the GA – not assumed – and is chosen from a database of four materials. The GA eliminates layers that do not contribute to the overall performance and therefore optimizes the size of the stacking. The results indicate that more solid material should be used closer to the hot plate (non-uniform distribution). Several nearly optimal configurations are found in the design space.

Keywords: Cooling of electronics; Heat sink; Cold plate; Layered structure; Genetic algorithms; Porous media

1. Introduction

The cooling of every heat-generating device (e.g., engine, electronics) is essential for maintaining its temperature in the acceptable range where the integrity and performance of the device are not jeopardized. The designer of a cooling system has to provide "thermal pathways" by which the heat current can be discharged in an external reservoir (e.g., ambient air) either by conduction, convection or radiation. The removal of heat by a coolant that sweeps or bathes a warm surface is one of the most encountered cooling strategies in engineering systems. Extended surfaces, or fins, are then used to increase the surface of exchange and maximize the heat transfer rate. Designing a fin system is equivalent to distributing a high thermal conductivity material within the flow or equivalently, distributing the flow within the high thermal conductivity material.

In this paper, we examine the opportunities for optimizing the performance of a cooling system made of a stack of porous layers, like the one shown in Fig. 1a. The coolant circulates in the network of pores and transports the heat outside of the system. The solid phase of the porous media is made of high thermal conductivity material in order to increase the surface of exchange and minimize the global thermal resistance of the stacking. Porous media, such as metallic foams and sponges, are used for improving the thermal performance of various systems [1–6]. One of the current challenges is the characterization of the porous material properties, such as the equivalent thermal conductivity and permeability [7–10].

Our approach is in line with the constructal point of view: the internal structure of the cooling system has to emerge as a result of the optimization, under global constraints [11]. Previous work on optimized internal structures in heat transfer systems led to the idea of 'designed porous media' [12,13]. A network of pores can be optimized for maximal heat removal or minimal pumping power requirement [14–19].

* Corresponding author. Tel.: +1 418 656 7829; fax: +1 418 656 7415.
E-mail address: Louis.Gosselin@gmc.ulaval.ca (L. Gosselin).

0017-9310/$ - see front matter © 2006 Elsevier Ltd. All rights reserved.
doi:10.1016/j.ijheatmasstransfer.2006.07.031

Nomenclature

Be	Bejan number
c_p	heat capacity, J kg^{-1} K^{-1}
c	cost per unit of mass, \$ kg^{-1}
C	cost per unit of length, \$ m^{-1}
D	diameter of the pipes
k	thermal conductivity, W m^{-1} K^{-1}
K	permeability, m^2
L	length, m
H	height, m
M′	mass per unit of length, kg m^{-1}
N	number of layers in the *y*-direction
P	pressure, Pa
q″	heat flux, W m^{-2}
S	number of cells in the *x*-direction
T	temperature, K
u	velocity, m s^{-1}
x, *y*	Cartesian coordinates, m

Greek symbols

α	thermal diffusivity, m^2 s^{-1}
ϕ	porosity
γ	penalty coefficient
μ	viscosity, kg m^{-1} s^{-1}
ρ	density, kg m^{-3}

Subscripts

f	fluid
j	layer index
s	solid
0	constraint value

Superscript

∼	dimensionless quantity

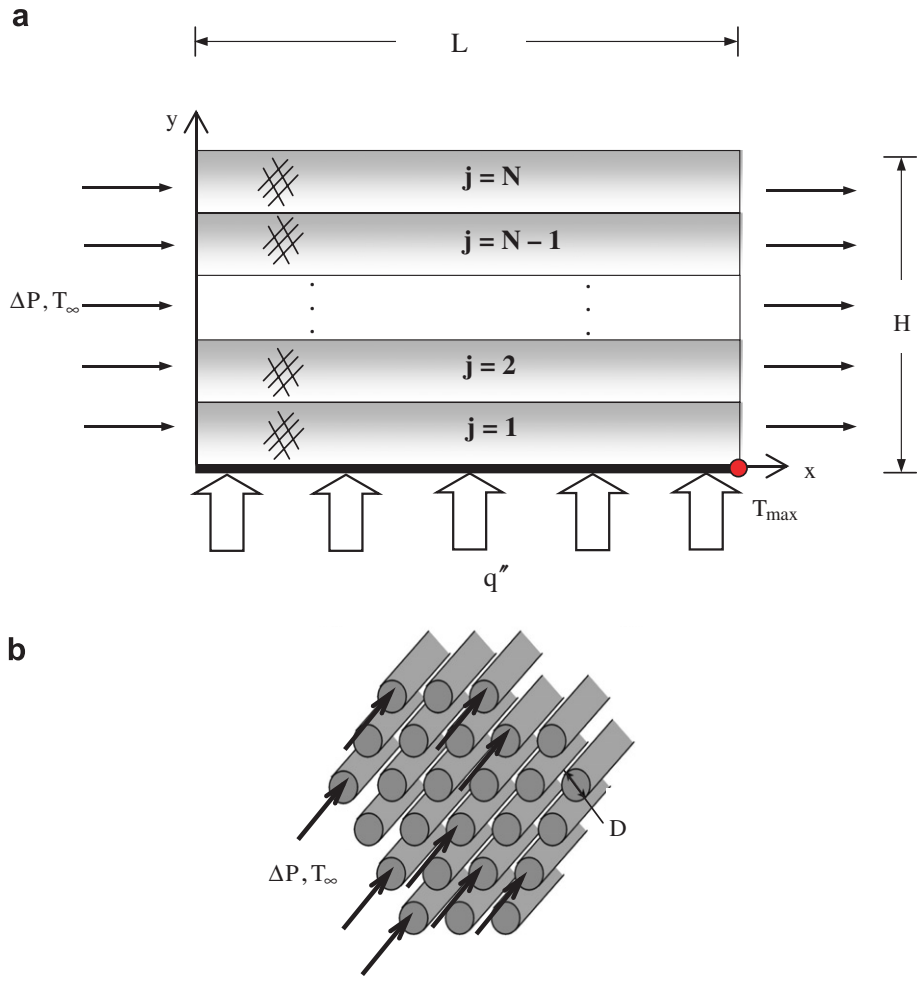

Fig. 1. Physical representation of (a) a stacking of porous layers and (b) the porous structure.

Other 'fluid–solid' structures used for cooling purposes have been optimized recently [20–25]. An optimization procedure for minimizing the thermal resistance of stacked micro-channel heat sink was proposed in Refs. [26–28]. The principal variables took into account were the fin aspect ratio, thickness, length of the heat sink and number of layers.

In this paper, we use genetic algorithms for optimizing the structure of a layered porous medium with a thermal objective in mind. Genetic algorithms have been used successfully by several authors for heat transfer problems [29,30]. An innovative aspect of this paper is that we optimize not only the porosity, but also the material composition of each layer for minimizing the temperature of a heat-generating plate, under global mass and cost constraints.

2. Mathematical model

In this section, we present a simple model for evaluating the heat transfer performance of a stack of porous layers used to remove heat from a warm plate as shown in Fig. 1a. The heat is carried through the solid part of the porous media, and is eventually dissipated in the fluid flow which transports the heat outside of the system. The model that we present in this section can also be used as a first approximation for representing a heat sink or a cold plate. One can vary the size, porosity, and materials within the cooling system for improving the performance.

On the bottom surface, we consider that a uniform heat flux q'' is applied. For example, heat-generating electronic components could be attached to that surface. Our objective is to cool down the heat-generating surface, i.e., to minimize the hot spot temperature $T_{\max}$. This is equivalent to minimizing the cooling system thermal resistance. For simplicity, we assume that the porous layers are made of bundles of small pores or tubes that are parallel to the flow (Fig. 1b). Therefore, the porosity of each layer is constant within the layer. This means that at a given position y, the ratios of the volume occupied by the solid and fluid phases are the same at every position x. The approach presented in this paper could be extended to other types of porous structures.

The fluid is driven trough the porous medium by a pressure difference ΔP between the inlet and outlet. For example, a fan could be positioned in front of the heat sink. One can use Darcy law for determining the volume-averaged velocity u in the layer j [31],

$$u_j = \frac{K_j \Delta P}{\mu L} \tag{1}$$

where K_j is the permeability of the layer j, and L is the length of the system. The permeability can be related to the porosity with the help of univocal $K(\phi)$-relations that depend on the internal structure of the porous medium [7–10]. In this paper, we rely on the relation $K_j(\phi_j) = \phi_j D^2/32$, appropriate for the chosen porous structure of Fig. 1b.

The geometry presented in Fig. 1b is such that the fluid velocity component in the y-direction is zero. Assuming that the transport of energy in the x-direction is dominated by convection, we can neglect the x-direction diffusion term in the equation of energy conservation, and obtain [31]:

$$(\rho c_p)_{\mathrm{f}} \frac{\partial (u_j T)}{\partial x} = \frac{\partial}{\partial y}\left(k_j \frac{\partial T}{\partial y}\right) \tag{2}$$

where k_j is the effective thermal conductivity of the porous structure in the y-direction and in the layer j. In the application considered here, the thermal conductivity of the solid phase is much larger than the one of the fluid. For example, we reported in Table 1 the solid-to-air conductivity ratios (at 300 K) of four materials. In each case, the ratios are much larger than one. Therefore, the value of k_j can be approximated by $k_{\mathrm{s}}(1-\phi)/(1+\phi)$ [32], which corresponds to the thermal conductivity in the direction perpendicular to the pores (y-direction). In other words, the tubes could be considered as inserts of negligible thermal conductivity [32]. Combining Eqs. (1) and (2), the energy equation becomes, in a dimensionless form,

$$Be \frac{\partial (\widetilde{K}\widetilde{T})}{\partial \tilde{x}} = \frac{\partial}{\partial \tilde{y}}\left(\tilde{k}\left(\frac{1-\phi}{1+\phi}\right)\frac{\partial \widetilde{T}}{\partial \tilde{y}}\right) \tag{3}$$

where

$$\tilde{x}, \tilde{y} = \frac{x, y}{L} \quad \widetilde{T} = \frac{T - T_0}{q'' L / k_{\mathrm{f}}} \quad \widetilde{K} = \frac{K}{L^2} \tag{4}$$

$$Be = \frac{L^2 \Delta P}{\alpha_{\mathrm{f}} \mu} \quad \tilde{k} = \frac{k_{\mathrm{s}}}{k_{\mathrm{f}}} \tag{5}$$

The Bejan number, Be, is a parameter that gives a measure of the pumping power available for driving the fluid through the porous layers. As indicated in Fig. 1a, the boundary condition at the inlet is $\widetilde{T} = 0$. The upper wall is assumed to be adiabatic, hence $\partial \widetilde{T}/\partial \tilde{y} = 0$. At the bottom surface where the heat flux is applied, we have the following dimensionless boundary condition:

$$\tilde{k}\left(\frac{1-\phi}{1+\phi}\right)\frac{\partial \widetilde{T}}{\partial \tilde{y}} = 1 \tag{6}$$

Finally, the permeability–porosity relation that we introduced in the beginning of the present section becomes, in a dimensionless form,

$$\widetilde{K} = \frac{K}{L^2} = \frac{1}{32}\phi\left(\frac{D}{L}\right)^2 = \frac{1}{32}\phi \widetilde{D}^2 \tag{7}$$

Table 1
Solid-to-air density and thermal conductivity ratios at 300 K [33] of four materials, and relative price per unit of mass [34]

Material	Density, $\tilde{\rho}$	Conductivity, $\tilde{k}$	Price, $\tilde{c}$
Aluminum (Al)	2327.5	9011.4	12.8
Copper (Cu)	7691.6	15247.2	18.9
Iron (Fe)	6776.3	3049.4	1
Brass (Br)	7663.2	3448.7	13

The objective function to minimize is the hot spot temperature, $\widetilde{T}_{\max}$, which is located at $\tilde{x} = 1$, $\tilde{y} = 0$. The hot spot is the weakest site from the thermal standpoint. To calculate the hot spot temperature, Eq. (3) needs to be solved, with the appropriate boundary conditions, and $\widetilde{K}(\phi)$-relation. The degrees of freedom (DOFs) are the porosity of each layers, ϕ_j, and the solid material used in each layer. The number of layers (N), the Bejan number (Be), and the size of the porous stacking ($\widetilde{H}$), are constant parameters that must be specified for the problem to be solved. The diameter of the pores (D) is non-designable, and therefore it is considered constant in the calculation of the permeability K. Larger diameters would be better as it would increase K, and the mass flow rate. However, if D becomes too large, the thermal equilibrium assumption (T_{solid}–T_{liquid}) would fail, and a two-temperature model would need to be employed.

To recognize that in every application, space, size and materials are expensive and limited, we pursue the minimization of $\widetilde{T}_{\max}$, under global mass and cost constraints. The density of the air is much smaller than the one of the solid phase materials, Table 1, and therefore, only the mass of the solid phase needs to be taken into account when evaluating the global mass of the stacking. In other words, the actual mass $\widetilde{M}$ of the heat sink is the summation of the mass of the solid phase of each porous layer. The value of $\widetilde{M}$ must be equal or smaller than a specified value $\widetilde{M}_0$ that we do not want to exceed,

$$\widetilde{M} = \frac{M'}{\rho_f L^2} = \sum_{j=1}^{N} \tilde{\rho}_j (1 - \phi_j) \Delta\tilde{y}_j \leqslant \widetilde{M}_0 \tag{8}$$

where $\Delta\tilde{y}_j$ is the thickness of the jth layer. It is also possible to consider a total cost constraint, which is the summation of the price associated with each layer,

$$\widetilde{C} = \sum_{j=1}^{N} \tilde{\rho}_j \tilde{c}_j (1 - \phi_j) \Delta\tilde{y}_j \leqslant \widetilde{C}_0 \tag{9}$$

where $\tilde{c}_j$ is the relative price per unit of mass. The values of $\tilde{c}_j$ for the four materials considered in this study are reported in Table 1. In Eq. (9), $\widetilde{C}_0$ is the threshold value of the total price that we do not want to exceed.

For respecting the definition of the porosity, the values of ϕ_j have to be in the interval [0, 1].

In summary, the purpose of this work is first to minimize the hot spot temperature, $\widetilde{T}_{\max}$, while respecting the mass and cost constraints, Eqs. (8) and (9), by varying the porosity and solid material of each layer composing the cooling device. When it is impossible to respect the mass and cost constraints with the specified number of layers and height of the system, the optimization process will tend to eliminate some layers by attributing them a porosity equal to one (void layer). The height of the system, $\widetilde{H}$, can thus be indirectly optimized in spite of the fact that it is a constant parameter in the problem, as mentioned before. Effects of this indirect optimization are shown in a further section.

3. Numerical modeling

The dimensionless energy equation, Eq. (3), has been discretized based on the finite volume approach [35]. The domain is meshed using S cells in the x-direction, that is S cells per unit of length. In the y-direction, we used the same density of cells, i.e., that we have at least $\widetilde{H}S$ nodes. The number N of porous layers is specified and therefore, each porous layer is represented by a certain number of computational layers of cells with the same properties (porosity, material). The value of S is chosen large enough so that further grid doubling leads to a hot spot temperature variation smaller than 1%. The cells are quadrilateral and are uniformly distributed in the domain. In order to have nodes directly on the boundary (where $T_{\max}$ lies) and keep a uniformly distributed grid, the thicknesses of the top and bottom layers of cells are half the one of the other layers [35]. For simplicity, we used uniform meshes as the computational times were not too long.

For the discretization of the left-hand side term of Eq. (3), an upwind scheme has been used: we approximated the temperature at the faces of the control volumes by the upwind temperature. This allows us to overcome the difficulty associated with the unspecified boundary condition at the outlet of the system, $\tilde{x} = 1$. The temperature distribution at the outlet is then delivered by the numerical model. For the discretization of the right-hand side term of Eq. (3), we use a harmonic mean to evaluate the effective thermal conductivity at the boundary of the control volumes [35].

Table 2
Mesh independence study for an aluminum heat sink, with $\widetilde{H} = 1$ and $\phi = 0.5$

S	$Be = 10^{11}$		$Be = 10^{15}$	
	$\widetilde{T}_{\max}$	$\left\lvert\frac{\widetilde{T}_{\max,i} - \widetilde{T}_{\max,i+1}}{\widetilde{T}_{\max,i+1}}\right\rvert$	$\widetilde{T}_{\max}$	$\left\lvert\frac{\widetilde{T}_{\max,i} - \widetilde{T}_{\max,i+1}}{\widetilde{T}_{\max,i+1}}\right\rvert$
15	7.2797×10^{-4}	–	1.6634×10^{-6}	–
30	7.3990×10^{-4}	1.6%	3.1369×10^{-6}	47%
60	7.4554×10^{-4}	**0.76%**	4.5770×10^{-6}	31%
120			5.0670×10^{-6}	9.7%
240			5.1703×10^{-6}	2%
480			5.1970×10^{-6}	**0.51%**

Table 3
Mesh independence study for an aluminum heat sink, with $\widetilde{H} = 1$ and $\phi = 0.9$

S	$Be = 10^{11}$		$Be = 10^{15}$	
	$\widetilde{T}_{\max}$	$\left\lvert\frac{\widetilde{T}_{\max,i} - \widetilde{T}_{\max,i+1}}{\widetilde{T}_{\max,i+1}}\right\rvert$	$\widetilde{T}_{\max}$	$\left\lvert\frac{\widetilde{T}_{\max,i} - \widetilde{T}_{\max,i+1}}{\widetilde{T}_{\max,i+1}}\right\rvert$
15	9.4958×10^{-4}	–	9.5673×10^{-7}	–
30	9.6445×10^{-4}	1.5%	1.9979×10^{-6}	52%
60	9.7112×10^{-4}	**0.69%**	3.9278×10^{-6}	49%
120			6.8101×10^{-6}	42%
240			9.0212×10^{-6}	25%
480			9.6000×10^{-6}	6.0%
960			9.7264×10^{-6}	1.3%
1920			9.7581×10^{-6}	**0.32%**

The resulting system of algebraic equations is then solved line-by-line with a tridiagonal solver. No iterative procedure is required due to the linearity of Eq. (3) and the known velocity profile. In other words, only one sweep in the x-direction is required. Therefore, for calculating the hot spot temperature for a given set of parameters, DOFs and constraints, one needs to solve S times a $\widetilde{H}S \times \widetilde{H}S$ tridiagonal matrix system.

In Table 2, we report an example of a mesh independence study for a typical case. We began with a given value for S, the number of cells in the x-direction. We kept the number of cells per unit length constant, and therefore we set the number of cells in the y-direction to $S\widetilde{H}$. We performed the numerical simulation and reported the value of the hot spot temperature in Table 2. Then we doubled the number of cells per unit length, we recalculated $\widetilde{T}_{\max}$ and we determined the relative difference in terms of $\widetilde{T}_{\max}$ compared with the previous "coarser" mesh. We continued to refine the mesh until further grid doubling resulted in relative differences in $\widetilde{T}_{\max}$ smaller than 1%. The study showed that 60 cells per unit length is an adequate choice for values of Be of up to 10^{13}. When Be is larger, the mesh needs to be denser. For $Be = 10^{14}$, the recommended number of cells per unit length is 240 and we need as many as 480 nodes per unit of length when $Be = 10^{15}$.

It is important to note that the required number of cells per unit of length for mesh independence varies with the porosity. We reported in Table 3 the mesh independence study for $\phi = 0.9$. We discovered that the required number of cells becomes larger when ϕ increased. When ϕ was set to 0.9, the required number of cells per unit of length were

Table 4
Parameters of the validation problem (thermal boundary layer limit)

Parameters	
Material	Aluminum
Fluid	Air
Number of layers (N)	1
Height of the system ($\widetilde{H}$)	5
Porosity (ϕ)	0.5
Pores diameter ($\widetilde{D}$)	0.001

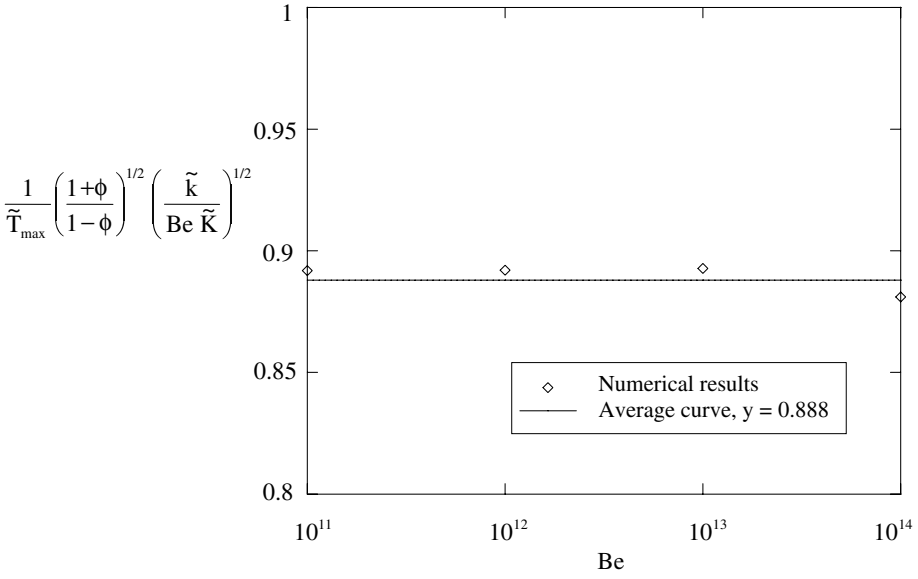

Fig. 2. Value of the left-hand side term of Eq. (11) as a function of the Bejan number.

60, 120, 240, 480 and 1920 for Bejan numbers of 10^{11}, 10^{12}, 10^{13}, 10^{14} and 10^{15}, respectively. Therefore, in the sections where the porosity distribution through the layers is optimized, the finest mesh must be used as ϕ can take any values between 0 and 1.

The code has been validated in the thermal boundary layer limit, for which an analytical solution exists when only one material and porosity are considered [31]. The height $\widetilde{H}$ of the stacking has been increased until the dimensionless temperature at the position $\tilde{x} = 1$ and $\tilde{y} = \widetilde{H}$ (upper right corner) reaches a value smaller than 1% of $\widetilde{T}_{\max}$. In that case, we can consider that the flow at that position has not felt the presence of the wall, which situation corresponds to the thermal boundary layer limit. The value found for $\widetilde{H}$ as well as the other parameters used for this validation problem are summarized in Table 4.

Based on the results presented in Ref. [31], we expect the following relation for the temperature distribution of the warm plate in the thermal boundary layer limit:

$$T_{\mathrm{p}}(x) = \frac{q''x}{0.886k(Pe_x)^{1/2}} + T_\infty \tag{10}$$

where $Pe_x = U_\infty x/\alpha$. In a dimensionless form, and recognizing that $\widetilde{T}_{\max}$ is located at $\tilde{x} = 1$, Eq. (10) can be rewritten as

$$\frac{1}{\widetilde{T}_{\max}}\left(\frac{1+\phi}{1-\phi}\right)^{1/2} Be^{-1/2}\widetilde{K}^{-1/2}\tilde{k}^{1/2} = 0.886 \tag{11}$$

We calculated the hot spot temperature with our code for several values of Be between 10^{11} and 10^{14}, and we plotted the value of the left-hand side term of Eq. (11). The result of this investigation is reported in Fig. 2. The average value of the left-hand side term of Eq. (11) obtained with our code was 0.888. The agreement between our results and the dimensionless correlation, Eq. (11), is within 0.25% for the values of Be investigated in this paper.

4. Optimization procedure

In the preceding sections, we presented how to evaluate numerically the objective function (hot spot temperature) and constraints (mass, cost) for a given set of degrees of freedom (porosity and material of each layer). The finite volume code has been coupled to an optimization toolbox relying on genetic algorithms (GA) [36]. The GA optimization toolbox is used for determining the optimal configuration of the cooling system in the design space. Due to the potentially large number of degrees of freedom, and to the need of optimally selecting the materials, genetic algorithms emerge as an appealing optimization approach compared with deterministic gradient-like methods. In this section, only a brief review of the GA is presented. Detailed description of the GA could be found elsewhere [36].

Each design is characterized by a set of $2N$ parameters. N genes characterize the porosity of each of the N layers, and another set of N genes determines the material of each layer. The porosity is free to vary between 0 and 1. The precision that we seek for the optimal porosity is determined by the number of bits that are used to express the porosity of a layer. For example, when the porosity of a layer is encoded with m bits, the precision is $1/(2^{\mathrm{m}})$. In this paper, we used 7 bits, which corresponds to a precision in terms of porosity of approximately 8×10^{-3}. In practice, the precision that we seek for the porosity is limited by the precision that we can achieve when building the layer.

The material is represented by an integer that is free to vary between 1 and 4, the number of potential materials, Table 1. Therefore, 2 bits are needed for expressing the material of a layer. In the end, a chromosome (i.e., a design) is made of the assembly of all the bits, and is thus $9N$-bit long. A chromosome representation is shown in top of Fig. 4. With as few as 8 layers (i.e., $N = 8$), there are $2^{72} = 10^{21}$ possible designs. The optimization strategy should be able to identify nearly optimal designs by evaluating only a small fraction of the possible designs.

The GA optimization procedure is described in Fig. 3. An initial population of 30 designs (i.e., chromosomes) is

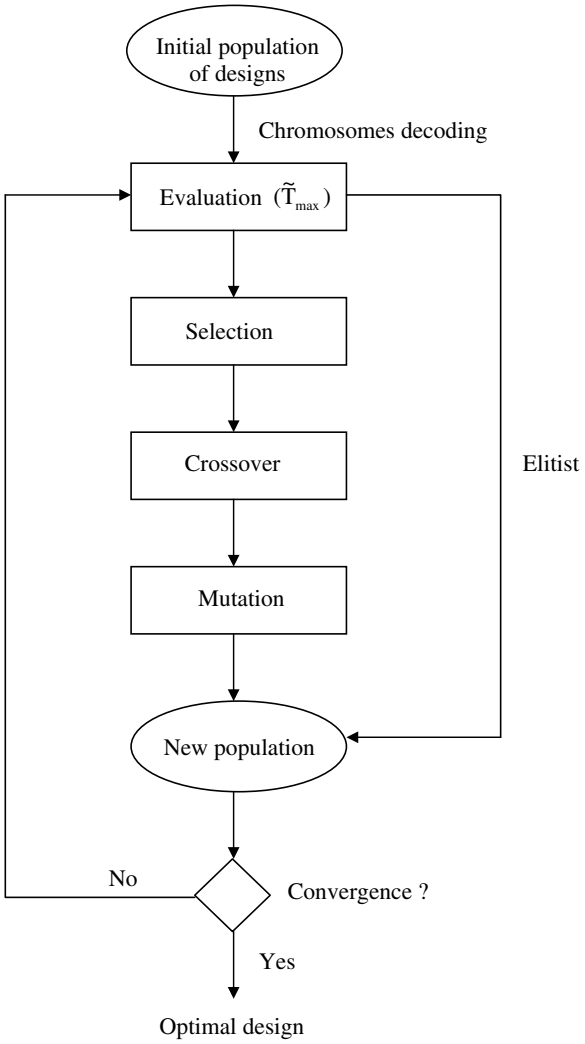

Fig. 3. Schematic of the GA procedure.

generated randomly. When the population has been generated, the GA decodes the chromosome of each individual to obtain its phenotypic values, which correspond to the decision variable values (i.e., porosities and materials). Having decoded the chromosome representation into the decision variable domain, the fitness of each individual ($\widetilde{T}_{\max}$) can be evaluated with the numerical procedure described in Section 3. Note that the complete GA procedure, except for the fitness evaluation, is always operated on the encoded chromosome.

The next step is the selection of the individuals that will have the chance to reproduce. In this paper, we used a stochastic universal sampling strategy (SUS) for which a detailed description is found in Ref. [36]. Since the selection is a probabilistic process, the fitter individuals will have more chances to get selected, although unfit ones could also be chosen. To take into account the mass and cost constraints, the objective function (hot spot temperature, $\widetilde{T}_{\max}$) is penalized in the following way:

$$F = \frac{\widetilde{T}_{\max}}{(Be\widetilde{D}^2)^{-1/2}} + \gamma_M \mathrm{MAX}\left[\left(\frac{\widetilde{M}-\widetilde{M}_0}{\widetilde{M}_0}\right),0\right] + \gamma_C \mathrm{MAX}\left[\left(\frac{\widetilde{C}-\widetilde{C}_0}{\widetilde{C}_0}\right),0\right] \quad (12)$$

where γ_M and γ_C are constants used to penalize the objective function when the mass and cost constraints are not respected, i.e., when $(\widetilde{M}-\widetilde{M}_0)>0$ or $(\widetilde{C}-\widetilde{C}_0)>0$. When the constraints are respected, we have $(\widetilde{M}-\widetilde{M}_0)<0$ and $(\widetilde{C}-\widetilde{C}_0)<0$, and the penalties vanish. Therefore, the GA procedure will tend to eliminate the designs that do not respect the constraints. As we can see in Eq. (12), the hot spot temperature has been normalized with $\left(Be\widetilde{D}\right)^{-1/2}$ to achieve values around 1. The factor $\left(Be\widetilde{D}\right)^{-1/2}$ is the scale of the hot spot temperature in the thermal boundary layer limit [31]. The penalty associated

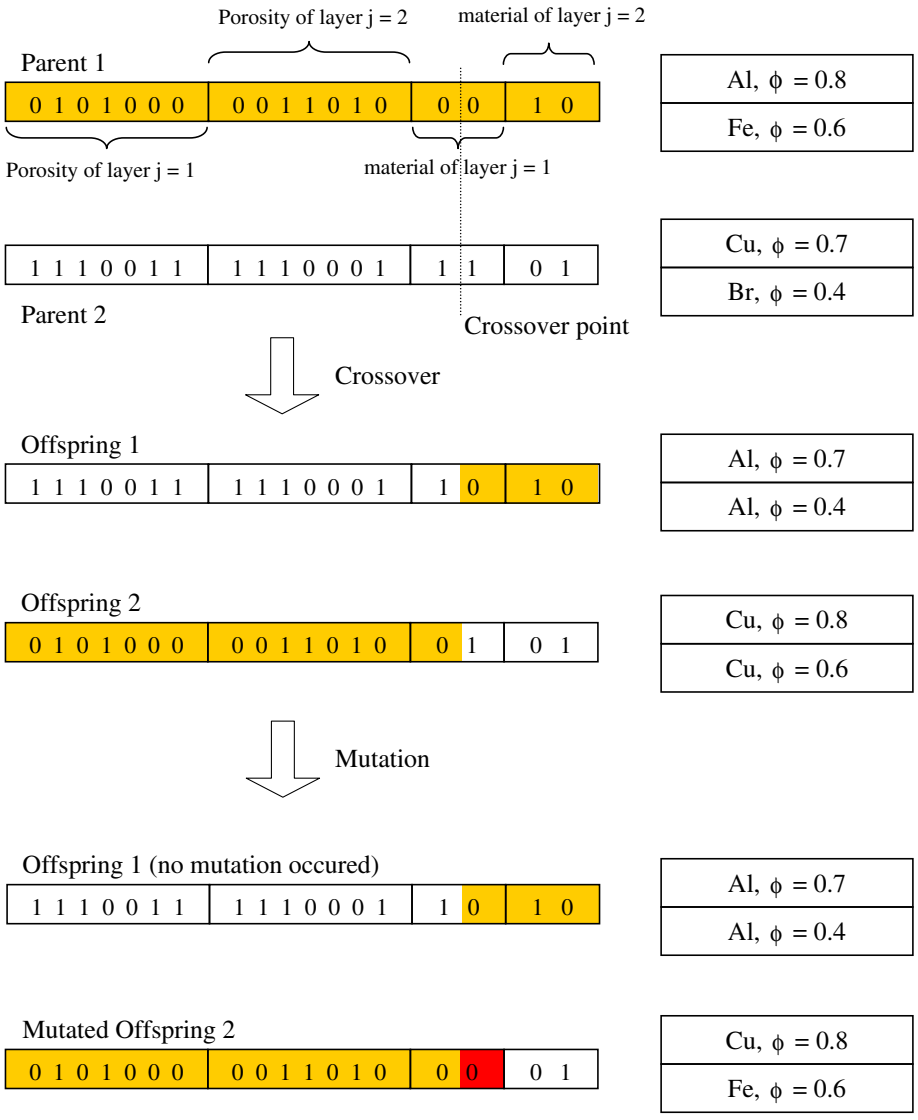

Fig. 4. Example of crossover and mutation for a two-layer system.

with the cost and mass constraints is also normalized to be in the vicinity of 1. This normalization of the hot spot temperature and constraints facilitates the choice of the penalty parameters γ_M and γ_C. These parameters have to be large enough for the program to eliminate a design that violates the constraints. On the other hands, too large a value of γ_M or γ_C will prevent the search of designs close to the constraint boundaries in the design space. The results reported in this paper were obtained with γ_M and γ_C set to 1.

Once the individuals have been selected, new individuals or designs are produced by the GA with a crossover operator. Like its counterpart in nature, crossover produces new individuals that receive information from both parents' genetic material. A simple crossover example with one crossover point is illustrated in Fig. 4. One crossover point is randomly selected to separate the chromosome of each parent into two segments of bits. The first segment of a parent is combined with the second segment of the other parent, and vice versa, in order to produce two offsprings. In this paper, we used three crossover points in such a way that each parent's chromosome is divided in four segments of bits. The positions of the crossover points are randomly chosen with a preset probability of 0.7.

Mutation is then randomly applied on chromosomes with low probability. The mutation modifies bits in the chromosome, resulting in a new design as shown in Fig. 4. We noted that when the mutation probability was too low (0.001), the GA tended to converge to local optima. For the results obtained in this paper, the probability was set to 0.04.

The last step of the GA procedure is the reinsertion of the new individuals in the population. In this paper, an elitist strategy was adopted. This means that the fittest designs of an initial population are ensured to propagate through the next generation. When the mutation process is completed, the offsprings that have just been created will replace the less fit individuals of the initial population. We set the number of fittest designs that are ensured to propagate to 3 (10% of the initial population). At that moment in the algorithm, the creation of the new population of designs is completed. This population becomes the initial population for the next generation and so on until the convergence criterion is reached (see Fig. 3). Because the GA is a stochastic search method, it is difficult to set a convergence criterion. In this paper, we terminate the GA after 200 consecutive generations without improvement of the best design, i.e., without decrease of $\widetilde{T}_{\max}$.

5. Effect of the stacking height for a given material

In this section, we examine the effect of the size of the stacking by varying its height, $\widetilde{H}$. The study is performed without constraints ($\gamma_M = \gamma_C = 0$) and for a specified material (aluminum). For several values of $\widetilde{H}$, the thermal resistance (i.e, $\widetilde{T}_{\max}$) of a four-layer system was minimized by the GA. In this case, the porosities are the only DOFs considered during the optimization process as the material is imposed. In Fig. 5, we reported the minimized hot spot temperature as a function of $\widetilde{H}$ for three different values of the Bejan number. It is important to understand that each point in Fig. 5 corresponds to the result of an optimization procedure. In fact, the procedure described in Section 4 has been conducted over a certain number of generations to obtain the value of each point ($\widetilde{T}_{\max,m}$). The subscript m refers to the minimized hot spot temperature. Fig. 5 reveals that for a given value of Be, $\widetilde{T}_{\max,m}$ decreases with $\widetilde{H}$ and eventually reaches a plateau. In other words, it makes no sense to increase indefinitely $\widetilde{H}$ as it would result in larger system with similar thermal resistance. Therefore, one can define an "efficient height" of the stacking such that increasing $\widetilde{H}$ further than that value will not yield a significant hot spot temperature decrease. Physically, the efficient height scales as the thickness of the thermal boundary layer, δ_T. When $H > \delta_T$, the portion of the system outside of the thermal boundary layer does not contribute to the heat removal. In Fig. 5, we read efficient heights around 3, 1.1 and 0.3 for $Be = 10^{11}$, $Be = 10^{12}$ and $Be = 10^{13}$, respectively. The reduction of the efficient height as the Bejan number increases is due to the decrease of the thermal boundary layer growing on the warm plate. Thereby, less material is needed (conduction effects are less important) to cool down the hot plate.

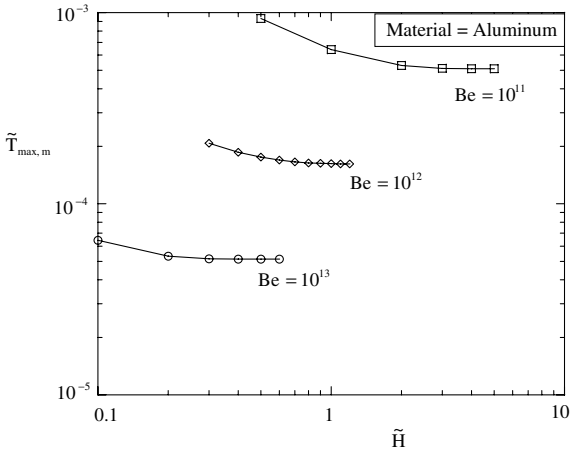

Fig. 5. Minimized hot spot temperature $\widetilde{T}_{\max,m}$ as a function of $\widetilde{H}$ for $Be = 10^{11}$, 10^{12} and 10^{13}.

6. Porosity distribution for a given material

Fig. 6 illustrates the optimal porosity assigned to each layer composing the system studied in Section 5 ($N = 4$), with $\widetilde{H} = 0.5$. For low Bejan numbers, the GA assigned higher porosities. That was a predictable result since a higher Bejan number means a higher velocity of the fluid through the porous structure. Because convection effects are less important for low Bejan numbers, the surface area should be greater to compensate. As shown in Fig. 6, layers are more porous far from the heat-generating wall. This is

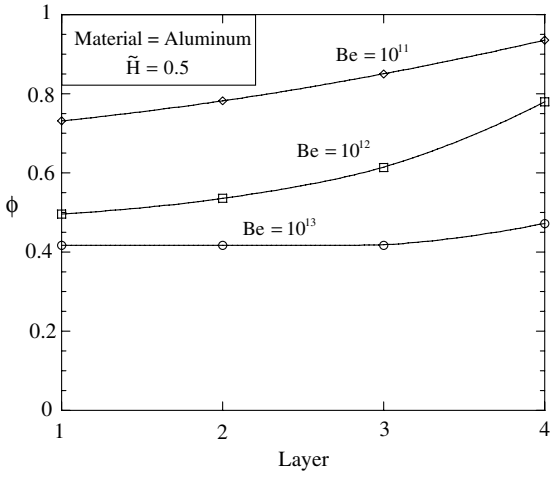

Fig. 6. Porosity distribution for a given material for $Be = 10^{11}$, 10^{12} and 10^{13}.

in accordance with Ref. [37,38], where a fin profile under global mass constraint is optimized. The optimal fin is thicker close to its base, and gets thinner as we move away from the base. In other words, it is better to put more solid material close to the wall.

The porosity distribution delivered by the GA when $Be = 10^{13}$ is such that the first three layers could be replaced by only one layer of porosity $\phi = 0.417$. We can explain this result by looking at Eq. (11). When $\widetilde{H} = 0.5$ and $Be = 10^{13}$, the heat sink works in the thermal boundary layer limit, as we can see in Fig. 5. Derivating $\widetilde{T}_{\max}$ with respect to ϕ in Eq. (11), and equaling to 0, we obtain a value of 0.414 for the optimal porosity in the thermal boundary layer limit. In view of the finite precision considered for the optimization of the porosity (7 bits), the theoretical and numerical results are in very good agreement. Because the heat sink does not work in the thermal boundary layer limit when $Be = 10^{11}$ and 10^{12}, the GA did not assign a constant porosity for these two cases as we can see in Fig. 6.

7. Optimal designs without constraint

In the last two sections, a material composition for the layers was imposed before we started the GA. Therefore, the designs generated by optimization were optimal only relative to the imposed material. If we want to generate fitter designs, we must let the GA attributing by itself the porosity-material combinations leading to the minimal hot spot temperature.

In this section, we considered a 10-layer system, giving more flexibility (freedom to morph) to the algorithm. For this reason, we performed four different simulations for each set of parameters in order to observe the repeatability of the results. In Tables 5–7, the optimal designs that were generated for three different Bejan numbers and their characteristics are presented. For this set of simulations, the required number of generations to converge varied between

Table 5
Optimization without constraints for $Be = 10^{11}$, $\widetilde{H} = 1$ and $\widetilde{D} = 0.001$

	Required number of generations	Configuration of layer j (material and porosity)										$\widetilde{M}$	$\widetilde{C}$	$\widetilde{T}_{\max,m} \times 10^4$
		1	2	3	4	5	6	7	8	9	10			
Simulation # 1	918	Cu 0.630	Cu 0.646	Cu 0.654	Cu 0.685	Cu 0.717	Cu 0.740	Cu 0.780	Cu 0.835	Cu 0.898	Cu 0.961	1894.9	35435	5.5469
Simulation # 2	861	Cu 0.638	Cu 0.646	Cu 0.661	Cu 0.693	Cu 0.717	Cu 0.748	Cu 0.787	Cu 0.843	Cu 0.890	Cu 0.961	1864.6	34869	5.5459
Simulation # 3	1279	Cu 0.630	Cu 0.646	Cu 0.669	Cu 0.693	Cu 0.709	Cu 0.756	Cu 0.795	Cu 0.835	Cu 0.882	Cu 0.953	1875.9	35080	5.5465
Simulation # 4	1115	Cu 0.630	Cu 0.646	Cu 0.677	Cu 0.685	Cu 0.717	Cu 0.748	Cu 0.787	Cu 0.835	Cu 0.898	Cu 0.953	1869.8	34965	5.5463

Table 6
Optimization without constraints for $Be = 10^{12}$, $\widetilde{H} = 1$ and $\widetilde{D} = 0.001$

	Required number of generations	Configuration of layer j (material and porosity)										$\widetilde{M}$	$\widetilde{C}$	$\widetilde{T}_{max,m} \times 10^4$
		1	2	3	4	5	6	7	8	9	10			
Simulation # 1	744	Cu 0.433	Cu 0.441	Cu 0.441	Cu 0.449	Cu 0.457	Cu 0.472	Cu 0.512	Cu 0.559	Cu 0.661	Cu 0.835	3652.9	68309	1.2620
Simulation # 2	936	Cu 0.433	Cu 0.433	Cu 0.441	Cu 0.449	Cu 0.466	Cu 0.480	Cu 0.512	Cu 0.559	Cu 0.654	Cu 0.819	3664.6	68528	1.2619
Simulation # 3	1522	Cu 0.433	Cu 0.433	Cu 0.441	Cu 0.449	Cu 0.457	Cu 0.480	Cu 0.504	Cu 0.567	Cu 0.654	Cu 0.827	3664.9	68533	1.2619
Simulation # 4	1056	Cu 0.433	Cu 0.433	Cu 0.441	Cu 0.449	Cu 0.465	Cu 0.480	Cu 0.512	Cu 0.551	Cu 0.654	Cu 0.827	3664.9	68533	1.2619

Table 7
Optimization without constraints for $Be = 10^{13}$, $\widetilde{H} = 1$ and $\widetilde{D} = 0.001$

	Required number of generations	Configuration of layer j (material and porosity)										$\widetilde{M}$	$\widetilde{C}$	$\widetilde{T}_{max,m} \times 10^5$
		1	2	3	4	5	6	7	8	9	10			
Simulation # 1	616	Cu 0.417	Cu 0.417	Cu 0.417	Cu 0.417	Cu 0.413	Cu 0.417	Cu 0.417	Cu 0.410	Cu 0.449	Al 0.236	4197.6	76782	3.9403
Simulation # 2	765	Cu 0.417	Cu 0.417	Cu 0.417	Cu 0.417	Cu 0.417	Cu 0.417	Cu 0.417	Cu 0.441	Cu 0.378	Cu 0.606	4351	81363	3.9403
Simulation # 3	826	Cu 0.417	Cu 0.417	Cu 0.417	Cu 0.417	Cu 0.417	Cu 0.417	Cu 0.417	Cu 0.417	Cu 0.402	Cu 0.480	4446.2	83145	3.9403
Simulation # 4	677	Cu 0.417	Cu 0.417	Cu 0.417	Cu 0.417	Cu 0.417	Cu 0.417	Cu 0.417	Cu 0.394	Cu 0.394	Cu 0.276	4625.4	86495	3.9403

616 and 1522 generations. Since the GA is a stochastic search method, the convergence speed depends on the way it explores the designs space.

As we can see, copper was assigned to all the layers. Because no mass and cost constraints were imposed, it is no surprise that the material with the highest thermal conductivity has been chosen, even if it is expensive and heavy (see Table 1). Moreover, we note that the repeatability of the results is excellent; the stacking configurations are slightly different but they all lead to similar cooling performances (values of $\widetilde{T}_{\max,m}$) for a given value of *Be*. The hot spot temperature decreases as the Bejan number (pumping power) increases. We also observe that the porosity distributions behave like in Section 6; layers become more porous as we move back from the hot plate and are also more porous for smaller values of *Be*.

When $Be = 10^{13}$, Table 7, the four designs that we obtained are exactly equivalent in terms of cooling performance, but have quite different masses and costs. In Section 5, we introduced the concept of "efficient height" of the stacking and we showed that increasing $\widetilde{H}$ further than that value would not yield a significant hot spot temperature decrease. When $\widetilde{H} = 1$ and $Be = 10^{13}$, the stacking is clearly oversized (see Fig. 5) and thus some porous layers are outside of the thermal boundary layer. These porous layers do not contribute to the removal of heat from the hot plate, but of course increase the global mass and cost of the system. In Table 7, we observe that the configurations of the 8th, 9th and 10th layers are somewhat different for the four simulations, which does not yield different values of $\widetilde{T}_{\max,m}$. The layers located inside the thermal boundary layer have the porosity $\phi = 0.417$, like the ones obtained in Section 6.

8. Mass and cost constrained optimal stacking

8.1. Mass constraint

In the previous section, the porous structure has been optimized without any mass or cost constraints. In other words, no requirement was formulated for the final mass of the system which may result in oversized system. In this section, we performed the optimization of the layered structure for $Be = 10^{11}$ under a global mass constraint. The penalty coefficient γ_M in Eq. (12) has been set to 1. We considered a critical mass value corresponding to 25% of the average mass of the optimized designs found in Section 5.3 (i.e., $\widetilde{M}_0 = 469.07$). Four simulations were performed and the results are reported in Table 8. The required number of generations to converge varied between 308 and 984.

We observed that the GA optimized each layer in order to generate a design which closely satisfies the mass constraint while keeping in mind that the objective is to minimize the hot spot temperature. The best design was found in Sim. # 2 with a $\widetilde{T}_{\max,m}$ value of 6.7051×10^{-4}. Compared with the designs optimized without constraints (Sec-

Table 8
Optimization under a mass constraint ($\widetilde{M}_0 = 469.07$) for $Be = 10^{11}$, $\widetilde{H} = 1$ and $\widetilde{D} = 0.001$

	Required number of generations	Configuration of layer j (material and porosity)										$\widetilde{M}$	$\widetilde{C}$	$\widetilde{T}_{max,m} \times 10^4$
		1	2	3	4	5	6	7	8	9	10			
Simulation # 1	308	Al 0.709	Al 0.732	Al 0.780	Al 0.680	Al 0.685	Al 0.780	Cu 0.937	Al 0.913	Al 0.945	Al 0.976	467.99	4648	6.8621
Simulation # 2	915	Al 0.654	Al 0.685	Al 0.717	Al 0.748	Al 0.756	Al 0.827	Al 0.874	Al 0.843	Al 0.929	Al 0.961	467.64	4162	6.7051
Simulation # 3	984	Cu 0.811	Al 0.764	Al 0.756	Al 0.756	Al 0.827	Al 0.827	Cu 0.945	Al 0.929	Al 0.929	Al 0.984	469.04	5924.9	6.9205
Simulation # 4	615	Al 0.661	Al 0.740	Al 0.732	Cu 0.882	Al 0.827	Al 0.811	Al 0.866	Al 0.874	Al 0.921	Al 0.945	468.55	5075.5	6.8559

tion 7), the GA changed the material composition from copper to aluminum for most layers in order to respect the mass constraint. We also note that the porosities are somewhat higher. By respecting the mass constraint, the thermal performance of the stacking necessarily drops since freedom to morph is lost due to the constraint. In fact, values of $\widetilde{T}_{\max,m}$ are almost 20% higher when the mass constraint is activated.

Even if the repeatability of the results presented in Table 8 is not as good as the one obtained when no constraint was considered, the thermal performances of the optimized designs vary only slightly. The maximal relative variation of $\widetilde{T}_{\max,m}$ between the four simulations is 2%. In other words, there are several nearly optimal designs (robustness).

8.2. Cost constraint

In this section, we do not consider the global mass of the system, but a requirement for the total cost is specified. We repeated the same procedure that we described in Section 8.1, with a critical cost of $\widetilde{C}_0 = 8771.81$ which represents 25% of the average cost of the designs obtained without constraints (Section 7). The new designs that we obtained are presented in Table 9. As we can see, the generated designs give almost the same value for $\widetilde{T}_{\max}$ (less than 1% of variation) and the best one is obtained in Sim. # 3 after 854 generations. This time, the porosities are somewhat smaller (more solid material) and at least one copper-made layer was attributed in each simulation. Since copper has the highest thermal conductivity, the closer it is from the hot plate, the more beneficial it is in terms of cooling. To be able to attribute the expensive copper-made layer next to the hot plate in Sim. # 3, the GA assigned one iron-made layer. The expensive cost of this copper-made layer must be counterbalanced with the use of a cheaper material elsewhere in the stacking. Finally, the $\widetilde{T}_{\max,m}$ values obtained are about 10% higher than the ones obtained without constraints.

8.3. Combined mass and cost constraints

At this stage, the architecture of the system was optimized under combined mass and cost constraints. The first case that was considered is the one for which $\widetilde{C}_0 = 8771.81$ (25% of the average cost obtained without constraints) and $\widetilde{M}_0 = 500$. When only the cost constraint $\widetilde{C}_0 = 8771.81$ was considered (Section 8.2), the lightest design delivered by the optimization weighs more than 500 (see Table 6). Therefore, no optimal design can closely satisfy both constraints. In Table 10, we reported our results for this particular case. The required number of generations to converge varied between 478 and 1105. As predicted, the mass values closely satisfied the mass constraint (limit of constraint), but the global costs were far below the constraint. When we compare Tables 9 and 10, we see that the GA attempted to replace copper and iron by aluminum in order to satisfy

Table 9
Optimization under a cost constraint ($\widetilde{C}_0 = 8771.81$) for $Be = 10^{11}$, $\widetilde{H} = 1$ and $\widetilde{D} = 0.001$

	Required number of generations	Configuration of layer j (material and porosity)										$\widetilde{M}$	$\widetilde{C}$	$\widetilde{T}_{\max,m} \times 10^4$
		1	2	3	4	5	6	7	8	9	10			
Simulation # 1	979	Al 0.567	Al 0.575	Al 0.5984	Al 0.630	Cu 0.772	Al 0.709	Al 0.724	Al 0.787	Al 0.866	Al 0.929	787.43	8758.6	6.2931
Simulation # 2	1801	Al 0.567	Al 0.591	Al 0.606	Al 0.614	Cu 0.772	Al 0.709	Al 0.748	Al 0.787	Al 0.850	Al 0.937	782.00	8710.2	6.2929
Simulation # 3	854	Cu 0.717	Al 0.606	Al 0.638	Al 0.646	Al 0.661	Al 0.701	Al 0.764	Al 0.795	Al 0.874	Fe 0.898	815.85	8742.1	6.2534
Simulation # 4	1295	Al 0.520	Al 0.535	Cu 0.803	Al 0.575	Al 0.661	Al 0.709	Al 0.772	Al 0.772	Al 0.882	Cu 0.969	776.53	8641.4	6.3166

Table 10
Optimization under combined mass and cost constraints ($\widetilde{C}_0 = 8771.81$ and $\widetilde{M} = 500$) for $Be = 10^{11}$, $\widetilde{H} = 1$ and $\widetilde{D} = 0.001$

	Required number of generations	Configuration of layer j (material and porosity)										$\widetilde{M}$	$\widetilde{C}$	$\widetilde{T}_{max,m} \times 10^4$
		1	2	3	4	5	6	7	8	9	10			
Simulation # 1	478	Al 0.669	Al 0.630	Al 0.701	Al 0.732	Al 0.748	Al 0.764	Al 0.827	Al 0.882	Al 0.929	Al 0.976	499.95	4449.5	6.6026
Simulation # 2	1105	Al 0.669	Al 0.677	Al 0.693	Al 0.701	Al 0.748	Al 0.795	Al 0.827	Al 0.858	Al 0.929	Al 0.961	499.64	4446.8	6.5963
Simulation # 3	748	Al 0.709	Al 0.654	Cu 0.827	Al 0.756	Al 0.803	Al 0.843	Al 0.858	Al 0.906	Al 0.937	Al 0.969	500.02	5778.0	6.7314
Simulation # 4	820	Al 0.638	Al 0.669	Al 0.693	Al 0.748	Al 0.724	Al 0.764	Al 0.835	Al 0.874	Al 0.929	Al 0.984	499.48	4445.4	6.6066

Table 11
Optimization under combined mass and cost constraints ($\widetilde{M}_0 = 469.07$ and $\widetilde{C}_0 = 1000$) for $Be = 10^{11}$, $\widetilde{H} = 1$ and $\widetilde{D} = 0.001$

	Required number of generations	Configuration of layer j (material and porosity)										$\widetilde{M}$	$\widetilde{C}$	$\widetilde{T}_{max,m} \times 10^3$
		1	2	3	4	5	6	7	8	9	10			
Simulation # 1	994	Al 0.866	Al 0.874	Fe 0.803	Fe 0.843	Al 0.953	Fe 0.874	Al 0.984	Fe 0.984	void 1.000	void 1.000	415.62	998.42	1.0262
Simulation # 2	691	Fe 0.677	Fe 0.780	Al 0.866	Al 0.929	Al 0.921	Fe 0.953	Fe 0.992	void 1.000	void 1.000	void 1.000	460.94	990.99	1.0858
Simulation # 3	946	Fe 0.677	Al 0.866	Al 0.913	Fe 0.827	Al 0.953	Al 0.969	Fe 0.976	Fe 0.976	void 1.000	void 1.000	436.63	996.13	1.0435
Simulation # 4	773	Fe 0.661	Al 0.835	Fe 0.858	Fe 0.890	Al 0.937	Al 0.945	void 1.000	void 1.000	void 1.000	void 1.000	465.46	995.51	1.1254

the constraint on the mass. Since an additional mass constraint was added to the initial cost constraint, it is also normal to observe a drop in the thermal performances from the designs presented in Table 9 to those presented in Table 10. In other words, $\widetilde{T}_{\max,m}$ values are higher in Table 10 because less freedom is given for the system to morph.

We then considered the following combination of constraints: $\widetilde{M}_0$ was set to 469.07 (25% of the average mass obtained without constraint) and $\widetilde{C}_0$ was set to 1000 (see Table 8). When only $\widetilde{M}_0 = 469.07$ was considered, the cheapest design was much more expensive than 1000 (see Table 8). The only way to satisfy the mass constraint was to attribute several aluminum-made layers to the designs. In fact, aluminum is by far the lightest material in Table 1, but it is also one of the most expensive. When one combines with this mass constraint a cost constraint as small as $\widetilde{C}_0 = 1000$, one can expect that the use of aluminum would be detrimental because of its high cost. In Table 11, we reported the results of the optimization under the new combined constraints $\widetilde{M}_0 = 469.07$ and $\widetilde{C}_0 = 1000$. To satisfy the cost constraint, the GA had no choice but to assign more iron (cheapest material). The best design was found after 994 generations (Sim. # 1) and possesses four iron-made layers. Unfortunately, iron is heavy and this is not desirable in view of the mass constraint.

Interesting to note is that to be able to satisfy both constraints at the same time, the GA removed some layers by attributing them a porosity of 1 (no solid material). In other words, the GA indirectly optimized the size of the system as well as the porosity and material of each layer in order to produce designs that respect both constraints. The emergence of void layers is a result of optimization and follows from the competition between the objective (minimize $\widetilde{T}_{\max}$) and constraints (mass and cost). The initial height $\widetilde{H}$ can be seen as an additional constraint: the stacking height has to be smaller (or equal) than $\widetilde{H}$. The system is free to morph within this domain, but can reduce its size if it is required to meet the constraint. In the case presented in Table 11, between 2 and 4 layers were removed to respect the constraints.

9. Conclusion

In this paper, we optimized a cooling system made of a stack of porous layers through which a coolant flows. We determine the optimal distribution of porosity, i.e., that we distribute optimally the channel flows and solid materials.

An innovative aspect is the determination of the materials of each layer. This would have been difficult with the use of gradient-like optimization methods. Material selection is an important potential of GA optimization methods in the field of thermal sciences.

Finally, we optimized the size of the cooling system (or equivalently, the number of stacked porous layers) as well. In general, cooling systems are optimized based on a specified size constraint. When there is a competition between different objectives, it is possible to dimension the cooling system. For example, in Ref. [39], the size of an electromagnet cooling system was optimized based on the competition between the magnetic and thermal performances. In this paper, the competition is between the call for a small overall mass, a small cost and the necessity of a low hot spot temperature, leading to a tradeoff architecture for the cooling system. Because it is difficult to define a proper value for the limiting cost C_0 or the limiting mass M_0 in Eqs. (8) and (9), an alternative approach would be a multi-objective optimization [40] of the temperature, mass and cost.

Further research could include a more refined analysis of the heat and fluid flow in the porous layers. Radiation effects on the heat transfer within the porous layers could have been taken into account. The internal structure of the porous media could have been varied and optimized. For example, a database of internal porous architectures (e.g., packed spheres, packed cylinders, straight channels) and their corresponding permeability–porosity and conductivity–porosity relations could be generated, and the optimization procedure could select the optimal internal structure of each layer.

Acknowledgement

L. Gosselin's work was supported by the Natural Sciences and Engineering Research Council of Canada (NSERC).

References

[1] B.M. Dempsey, S. Eisele, D.L. McDowell, Heat sink applications of extruded metal honeycombs, Int. J. Heat Mass Transfer 48 (3–4) (2005) 527–535.
[2] T. Fend, R. Pitz-Paal, O. Reutter, J. Bauer, B. Hoffschmidt, Two novel high-porosity materials as volumetric receivers for concentrated solar radiation, Solar Energy Mater. Sol. Cells 84 (2004) 291–304.
[3] J.J. Hwang, G.J. Hwang, R.H. Yeh, C.H. Chao, Measurement of interstitial convective heat transfer and frictional drag for flow across metal foams, J. Heat Transfer 124 (2002) 120–129.
[4] K.-H. Ko, N.K. Anand, Use of porous baffles to enhance heat transfer in a rectangular channel, Int. J. Heat Mass Transfer 46 (22) (2003) 4191–4199.
[5] Y.-T. Yang, C.-Z. Hwang, Calculation of turbulent flow and heat transfer in a porous-baffled channel, Int. J. Heat Mass Transfer 46 (5) (2003) 771–780.
[6] S. Chikh, A. Boumedien, K. Bouhadef, G. Lauriat, Heat transfer enhancement by porous substrate addition on the inner wall of a tubular heat exchanger, Revue générale de thermique – Int. J. Therm. Sci. 36 (1) (1997) 41–50.
[7] J. Tian, T. Kim, T.J. Lu, H.P. Hodson, D.T. Queheillalt, D.J. Sypeck, H.N.G. Wadley, The effects of topology upon fluid-flow and heat-transfer within cellular copper structures, Int. J. Heat Mass Transfer 47 (2004) 3171–3186.
[8] J.G. Fourie, J.P. Du Plessis, Effective and coupled thermal conductivities of isotropic open-cellular foams, Am. Inst. Chem. Eng. J. 50 (3) (2004) 547–556.
[9] A.K. Al-Hadharami, L. Elliot, D.B. Ingham, W. Wen, Flows through horizontal channels of porous materials, Int. J. Energy Res. 27 (2003) 875–889.

[10] C.-W. Nan, R. Birringer, D.R. Clarke, H. Gleiter, Effective thermal conductivity of particulate composites with interfacial thermal resistance, J. Appl. Phys. 81 (10) (1997) 6692–6699.
[11] A. Bejan, Shape and Structure, from Engineering to Nature, Cambridge university Press, Cambridge, UK, 2000.
[12] A. Bejan, Designed porous media: maximal heat transfer density at decreasing length scales, Int. J. Heat Mass Transfer 47 (14–16) (2004) 3073–3083.
[13] J.C. Ordonez, A. Bejan, R.S. Cherry, Designed porous media: Optimally nonuniform flow structures connecting one point with more points, Int. J. Therm. Sci. 42 (9) (2003) 857–870.
[14] W. Wechsatol, S. Lorente, A. Bejan, Dendritic heat convection on a disc, Int. J. Heat Mass Transfer 46 (23) (2003) 4381–4391.
[15] L. Gosselin, A. Bejan, Tree networks for minimal pumping power, Int. J. Therm. Sci. 44 (01) (2005) 53–63.
[16] M.R. Errera, A. Bejan, Tree networks for flows in composite porous media, J. Porous Media 2 (1) (1999) 1–17.
[17] L. Gosselin, A. Bejan, Emergence of asymmetry in constructal tree flow networks, J. Appl. Phys. 98 (10) (2005).
[18] L. Gosselin, Fitting the flow regime in the internal structure of heat transfer systems, Int. Commun. Heat Mass Transfer 33 (1) (2005) 30–38.
[19] L. Gosselin, Minimum pumping power fluid tree networks without a priori flow regime assumption, Int. J. Heat Mass Transfer 48 (11) (2005) 2159–2171.
[20] K. Park, D.-H. Choi, K.-S. Lee, Numerical shape optimization for high performance of a heat sink with pin-fins, Numer. Heat Transfer; Part A: Appl 46 (9) (2004) 909–927.
[21] K. Park, D.-H. Choi, K.-S. Lee, Optimum design of plate heat exchanger with staggered pin arrays, Numer. Heat Transfer; Part A: Appl. 45 (4) (2004) 347–361.
[22] S.Y. Kim, A.V. Kuznetsov, Optimization of pin-fin heat sinks using anisotropic local thermal nonequilibrium porous model in a jet impinging channel, Numer. Heat Transfer; Part A: Appl. 44 (8) (2003) 771–787.
[23] C.H. Huang, J.H. Hsiao, An inverse design problem in determining the optimum shape of spine and longitudinal fins, Numer. Heat Transfer; Part A: Appl. 43 (2) (2003) 155–177.
[24] B.A.-K. Abu-Hijleh, Optimization of natural convection heat transfer from a cylinder with high conductivity fins, Numer. Heat Transfer; Part A: Appl. 43 (1) (2003) 65–82.
[25] S.H. Ha, S. Cho, Topological shape optimization of heat conduction problems using level set approach, Numer. Heat Transfer; Part B: Appl. 48 (1) (2005) 67–88.
[26] K. Jeevan, G.A. Quadir, K.N. Seetharamu, I.A. Azid, Z.A. Zainal, Optimization of thermal resistance of stacked micro-channel using genetic algorithms, Int. J. Numer. Methods Heat Fluid Flow 15 (1) (2005) 27–42.
[27] D. Liu, S.V. Garimella, Analysis and optimization of the thermal performance of microchannel heat sinks, Int. J. Numer. Methods Heat Fluid Flow 15 (1) (2005) 7–26.
[28] X.J. Wei, Y. Joshi, Optimization study of stacked micro-channel heat sinks for microelectronic cooling, IEEE Trans Compon. Pack. Technol. 26 (2003) 55–61.
[29] I. Ozkol, G. Komurgoz, Determination of the optimum geometry of the heat exchanger body via a genetic algorithm, Numer. Heat Transfer; Part A: Appl. 48 (3) (2005) 283–296.
[30] M. Younes, A. Potiron, A genetic algorithm for the shape optimization of parts subjected to thermal loading, Numer. Heat Transfer; Part A: Appl. 39 (5) (2001) 449–470.
[31] A. Bejan, Convection Heat Transfer, third ed., Wiley, New York, 2004, Chapter12.
[32] D.C. Pham, S. Torquato, Strong-contrast expansions for the effective conductivity of isotropic multiphase composites, J. Appl. Phys. 94 (2003) 6591–6602.
[33] F.P. Incropera, D.P. DeWitt, Fundamentals of Heat and Mass Transfer, fifth ed., Wiley, 2002.
[34] www.metalprices.com, as of October 26, 2005.
[35] S.V. Patankar, Numerical Heat Transfer and Fluid Flow, Hemisphere, 1980.
[36] C.R. Houck, J.A. Joines, M.G. Kay, A Genetic Algorithm for Function Optimization: A Matlab Implementation, ACM Transactions on Mathematical Software, 1996.
[37] F. Bobaru, S. Rachakonda, Optimal shape profiles for cooling fins of high and low conductivity, Int. J. Heat Mass Transfer 47 (2004) 4953–4966.
[38] P. Jany, A. Bejan, Ernst Schmidt's approach to fin optimization: an extension to fins with variable conductivity and the design of ducts for fluid, Int. J. Heat Mass Transfer 31 (1998) 1635–1644.
[39] L. Gosselin, A. Bejan, Constructal thermal optimization of an electromagnet, Int. J. Therm. Sci. 43 (2004) 331–338.
[40] R. Hilbert, G. Janiga, R. Baron, D. Thévenin, Multi-objective shape optimization of a heat exchanger using parallel genetic algorithms, Int. J. Heat Mass Transfer 49 (15–16) (2006) 2567–2577.